

Pd Nanoparticles Supported on Tungsten Carbide Embedded onto Ordered Mesoporous Carbons for Electrocatalysis of Formic Acid Oxidation

Liangliang Zou^{1,2}, Mingjun Ren^{1,2}, Haifeng Zhang¹, Zhiqing Zou¹, Hui Yang^{1, *}, Songlin Feng¹

¹ Shanghai Advanced Research Institute, Chinese Academy of Sciences (CAS), Shanghai 201210, China

² Graduate University of the CAS, Beijing 100039, China

*E-mail: yangh@sari.ac.cn; huiyang65@hotmail.com

Received: 21 February 2013 / Accepted: 3 April 2013 / Published: 1 May 2013

In this work, tungsten carbide (WC) embedded onto ordered mesoporous carbons (OMCs) is used as the support of Pd nanoparticles for electrocatalytic oxidation of formic acid. The WC loaded OMCs was prepared via a hard template route. Pd nanoparticles were then deposited on the support by a modified ethylene glycol reduction. The obtained catalysts were characterized by high-resolution transmission electron microscopy, X-ray diffraction, N₂ adsorption–desorption and electrochemical measurements. It is found that the composite of WC nanoparticles loaded OMCs maintains the highly ordered mesoporous structure of the template. Although the Pd/OMCs and Pd-WC/OMCs catalysts have a similar Pd particle size, the latter exhibits an enhanced electrocatalytic performance for formic acid oxidation in comparison with the Pd/OMCs and commercial Pd/C catalysts, suggesting a promotion effect of Pd nanoparticles by WC. The improved electrocatalytic performance of formic acid oxidation on the Pd-WC/OMCs may be ascribed to a synergistic effect between Pd nanoparticles, the WC component, and to the structural effect of the OMCs.

Keywords: Tungsten carbide; Mesoporous carbon; Pd nanoparticles; Formic acid oxidation

1. INTRODUCTION

Recently, formic acid has attracted much attention as a promising alternative fuel for direct liquid fuel cells [1,2] due to its various advantages, such as lower toxicity, diminished poisoning of Pt-based electrocatalysts, and lower crossover than methanol through the Nafion membrane. On the other hand, as a result of the lower cost and higher catalytic activity toward formic acid electrooxidation, as compared to those of Pt-based nanoparticles [3,4], high-performance Pd-based nanoparticles have

assumed enhanced attention in the literature [5-7]. The incorporation of some metals, such as Co [8], Ir [9], Pb [10], P [11] and B [12], into the Pd/C catalyst has resulted in enhanced activity for formic acid oxidation. However, both catalytic activity and durability continued to require improvement in order to enable the practical application of such modified catalysts in direct formic acid fuel cells (DFAFC).

Tungsten carbide-based (i.e., WC-based) materials have aroused considerable interest in recent years because of their resemblance to platinum in various catalytic reactions [13]. To this end, WC has been used as electrocatalysts' support for the oxidation of methanol [14-16], ethanol [17,18], hydrogen [19], and also for the oxygen reduction reaction (ORR) in both acidic and alkaline solutions [19-21]. The metal-modified WC electrocatalysts have also shown an increased CO tolerance [15]. To further improve catalytic performance, WC with a variety of morphologies have been prepared and used as supports for electrocatalysts [23-25]. For example, Wang et al. [26] synthesized a WC/graphitic carbon nanocomposite via an in-situ synthetic route at 1000°C. The catalytic activity of the Pt-WC/graphitic catalyst is about two times higher than that of Pt/C for the ORR. Ganesan et al. [27] investigated platinumized mesoporous WC for methanol oxidation. WC was found to be more than just a support for Pt nanoparticles, but also as an active phase working together with Pt for methanol oxidation. Hu et al. [18] prepared Pd catalysts supported on WC/multi-walled carbon nanotubes (MWCNTs). Their results were interpreted as indicating a synergistic effect between Pd nanoparticles, WC, and MWCNTs (the latter principally a structural effect) results in high performance of the Pd catalysts for ethanol oxidation. Unfortunately, the WC-based materials show low surface area and nonuniform mesostructures. The former probably makes them unsuitable as an electrocatalysts' support and the latter seriously diminishes the impact of the mesoporous character in facilitating chemical reactions [28].

It is known that ordered mesoporous carbons (OMCs) possess good electrochemical properties [29], and may be used, potentially, as catalyst supports in fuel cells due to their appealing structural characteristics, such as periodic and uniform mesopores and high surface area [30-33]. Mesoporous carbons with 3D ordered pore structures also might promote the mass transport of both reactants and by-products during fuel cell operation. For example, Ryoo and coworkers [34], described a general strategy for the synthesis of highly ordered, rigid arrays of mesoporous carbon with uniform but tunable pore diameters (typically 6 nm inside and 9 nm outside). The resultant material supports a highly dispersion of platinum nanoparticles and shows improved ORR electrocatalysis, originating, respectively, from a higher surface area and a highly ordered mesopore structure.

Considering the advantages of the OMCs and WC, a composite of WC and OMCs has been used as the catalyst support for fuel cell reaction. As an example, Wang et al. [28] synthesized mesoporous carbon/WC composite nanomaterials with a surface area 538 m²/g by the soft-template method. The Pt nanoparticles supported on OMC/WC demonstrated a better performance than the commercial PtRu/C for methanol electrooxidation. However, the intrinsic ordered within the OMC/WC composite can be improved. In this work, using a unique hard template method, we have developed a composite of WC embedded onto OMC with a highly ordered mesoporous structure and a surface area of 1098 m²/g. We have used this composite as the support for Pd nanoparticles for formic acid oxidation. The electrocatalytic performance for formic acid oxidation was evaluated by cyclic voltammetry (CV) and chronoamperometric (CA) method.

2. EXPERIMENTAL PART

2.1 Sample preparation

2D hexagonally ordered mesoporous silicas (SBA-15) was synthesized according to a previously established method [35], using a triblock polymer (Pluronic P123) as a structure-directing agent and tetraethylorthosilicate (TEOS) as a silica source. WC-containing ordered mesoporous carbon (WC/OMCs) was obtained by incipient wetting impregnation of SBA-15 silica as described in the literature [36]. Different from the conventional template-replication method, small amount of phosphotungstic acid (PWA; $\text{H}_3\text{PO}_4\text{W}_{12}\cdot x\text{H}_2\text{O}$) was added along with sucrose, the weight ratio of PWA:sucrose = 1:25. The mixture of PWA/carbon/SBA-15 was calcined at 900 °C for 2 h with an Ar flow for carbonization. The SBA-15 was removed by stirring the silica/carbon composites in 10% HF solution for 24 h, followed by washing with deionized water and drying overnight under vacuum at 60 °C. The OMCs were synthesized with a similar procedure, but without the addition of PWA.

Palladium nanoparticles at 30 wt.% loading were deposited on the OMCs and WC/OMCs via a modified ethylene glycol (EG) reduction route [37]; in this process trisodium citrate (TC) was used as complexing agent and stabilizer. Typically, 70 mg WC/OMCs, 333 mg TC and 30 mL Na_2PdCl_4 (1mg Pd mL^{-1}) were homogeneously dispersed in 20 mL of ethylene glycol under vigorous stirring. Under an nitrogen atmosphere, the solution was refluxed at 120 °C for 4h with continuous stirring. Following the reaction, the resultant powder was filtered, washed with water, and then dried overnight under vacuum at 60 °C. The commercial carbon-supported 40 wt.% Pd catalyst purchased from BASF, referred to as Pd/C, was used as the reference sample for structural and electrochemical characterization.

2.2 Physical characterization

The analysis of the WC content within the WC/OMCs was performed with an Axis X-ray spectrometer. Powder X-ray diffraction (XRD) measurements were conducted using a Bruker AXS D8 Advance Powder X-ray Diffractometer, with a Cu $\text{K}\alpha$ ($\lambda = 1.5418 \text{ \AA}$) radiation source operating at 40 kV and 40 mA. Large and small angle radiations were obtained at scanning rates of 2° min^{-1} and 1° min^{-1} , respectively. Transmission electron microscopy (TEM) images were obtained with a JEOL 2100F at an acceleration voltage of 200 kV. Prior to observation, the samples were sonicated in absolute ethanol for 10 min, then dropped onto a holey carbon film supported on a copper grid.

Nitrogen adsorption of the sample was measured at 77 K using a Micromeritics ASAP 2020. Prior to the measurement, the samples were degassed at 200 °C for about 5 h. The specific surface area of the samples was evaluated by the Brunauer–Emmett–Teller (BET) method using adsorption data in a relative pressure (P/P₀) range from 0.05 to 0.3. The pore size distributions of the samples were calculated from the adsorption branch using Barrett-Joyner-Halenda (BJH) method. The total pore volume was estimated from the adsorbed amount at the relative pressure of 0.99.

2.3 Electrochemical characterization

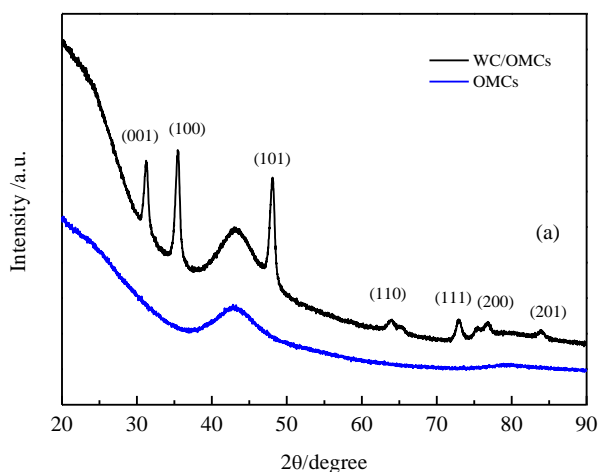
The performance of Pd catalysts loaded onto different supports for the formic acid oxidation reaction at a temperature of ca. 25°C was evaluated by cyclic voltammetry (CV) using a conventional three-electrode electrochemical cell with a Solartron Electrochemical Interface controller (SI1287). Along with the working electrode, a glassy carbon plate was used as the counter electrode, and a saturated calomel electrode (SCE) as the reference electrode. All potential data, however, are referred to the reversible hydrogen electrode (RHE).

Porous working electrodes were prepared as follows: 10 mg of the catalyst, 0.5 ml of Nafion (5 wt%, Aldrich) and 2.5 ml of ultrapure water were mixed ultrasonically. Then 3 μ l of this ink was transferred onto a glassy carbon disk (3 mm in diameter) and left to dry overnight. Such an electrode contained ca. 70.7 μ gcm⁻² of Pd. The electrolyte for formic acid oxidation consists of 0.1 M formic acid and 0.1 M HClO₄. The CVs were recorded at a potential scanning rate of 50 mV/s. The real electrochemical surface areas (ECSAs) of the catalysts were determined by CO_{ad} oxidation using CO stripping voltammetry. The oxidation charge of monolayer adsorption of CO on the Pd surface was assumed to be 420 μ Ccm⁻² [35]. High purity nitrogen was used for deaeration of the solution. During measurements a gentle gas flow was kept above the electrolyte.

3. RESULTS AND DISCUSSION

The content analysis of WC by X-ray spectrometer indicated ca. 10.7% of WC within the WC/OMCs, which is nearly equal to the stoichiometric ratio of the precursor mixture.

Wide angle XRD patterns of the OMCs and WC/OMCs are shown in Fig. 1(a). For WC/OMCs, the diffraction peaks at 31.4°, 35.6°, 48.4°, 65.5°, 72.9°, 76.8° and 84.0° correspond, respectively, to (0 0 1), (1 0 0), (1 0 1), (1 1 0), (1 1 1), (2 0 0) and (2 0 1) facets for a hexagonal WC phase (PDF#89-2727), suggesting that the WC phase is highly crystalline, while those at 23° and 46° correspond to diffraction facets of mesoporous carbon.



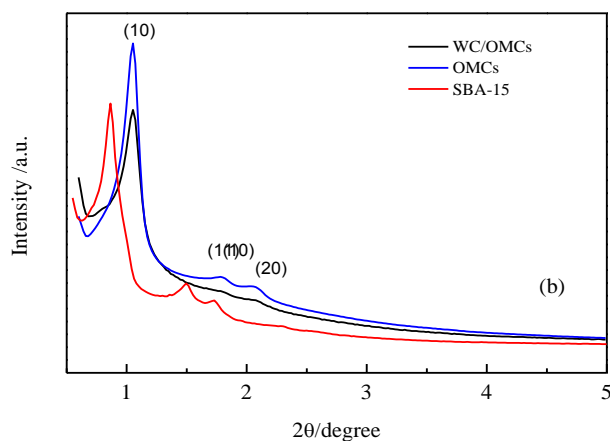


Figure 1. XRD patterns of WC/OMCs and OMCs (a). And small angle XRD patterns of SBA-15, WC/OMCs and OMCs (b)

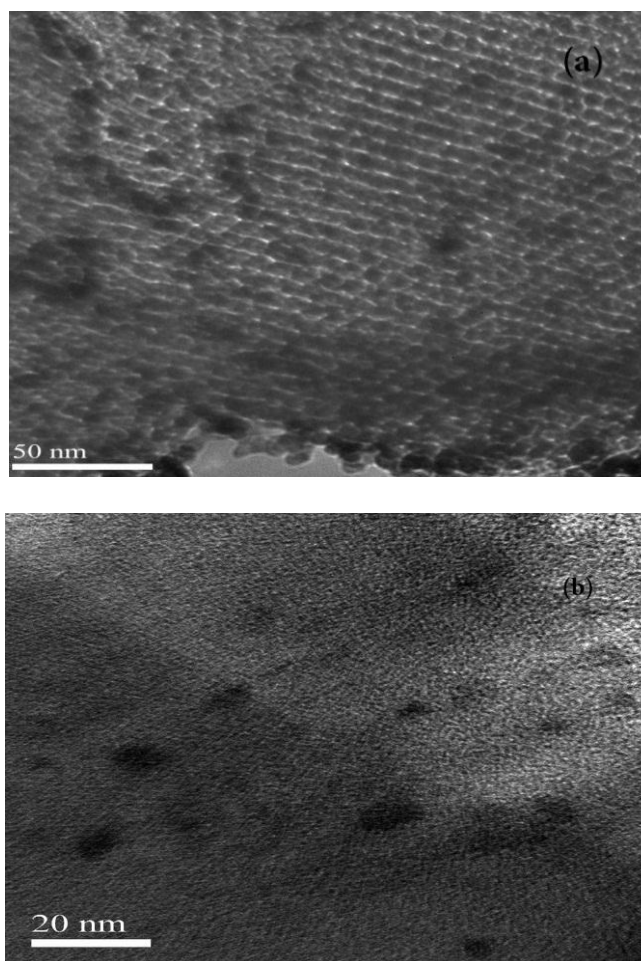


Figure 2. TEM images of WC/OMCs samples: (a) the mesoporous structure and (b) the WC nanoparticles

Small angle XRD patterns results are displayed in the inset on Fig.1(b). The SBA-15 template displays three-resolved peaks, which can be assigned to (10), (11) and (20) reflections characteristic of

2D hexagonal space group $p6mm$. The small angle XRD patterns of the WC/OMCs and OMCs show similar diffraction to the SBA-15 template, indicating that the resultant WC/OMCs and OMCs materials replicates the 2D hexagonal ordered structure of the parent SBA-15. Parallel channels can be clearly observed on the TEM image of WC/OMCs shown in Fig. 2a, which confirms that WC/OMCs possess a delicate, ordered surface structure. Fig. 2b also shows the TEM image of WC/OMCs. It is found that WC, with a mean diameter of ca. 9 nm, is well distributed onto the OMCs. However, due to a strong dark/bright contrast between WC and OMCs during the TEM measurement, the mesoporous structure of WC/OMCs cannot be clearly seen.

Table 1. Structural parameters of SBA-15, WC-OMCs and OMCs

	$S_{\text{BET}}(\text{m}^2/\text{g})$	$V_t (\text{cm}^3/\text{g})$	$D_{\text{BJH}}(\text{nm})$
SBA-15	745	1.27	9.2
OMCs	1633	1.64	4.1
WC/OMCs	1098	1.14	4.3

S_{BET} is the specific surface area calculated from BET method at relative pressure of 0.05–0.3; V_t is the total volume calculated at relative pressure of 0.99; D_{BJH} is the pore diameter at maximum of the pore size distribution calculated by BJH method from the adsorption branch.

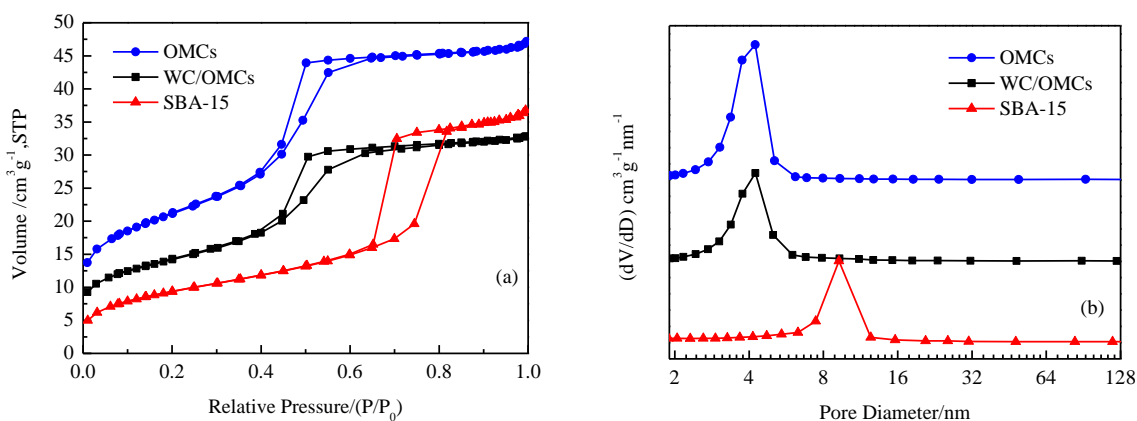


Figure 3. Nitrogen adsorption isotherms of SBA-15, WC/OMCs and OMCs (a), and (b) their corresponding BJH pore size distributions.

The nitrogen adsorption isotherms of SBA-15, WC/OMCs and OMCs are shown in Fig. 3a, and the structural parameters derived from them are listed in Table 1. All three materials display type-IV isotherms with an H2 hysteresis loop that has a distinct condensation step at P/P_0 , indicative of a uniform mesoporous structure. The surface areas and total pore volumes of the OMCs are $1633 \text{ m}^2\text{g}^{-1}$ and $1.64 \text{ cm}^3\text{g}^{-1}$, respectively; which are larger than those for the WC/OMCs ($1098 \text{ m}^2\text{g}^{-1}$ and $1.14 \text{ cm}^3\text{g}^{-1}$, respectively). The BJH pore size distributions of SBA-15, WC/OMCs and OMCs, calculated from the adsorption branch, are shown in Fig. 3b. A narrow pore-size distribution is centered at 9.2 nm

for SBA-15, while the pore-size distributions are centered at 4.3 nm for WC/OMCs and 4.1 nm for OMCs.

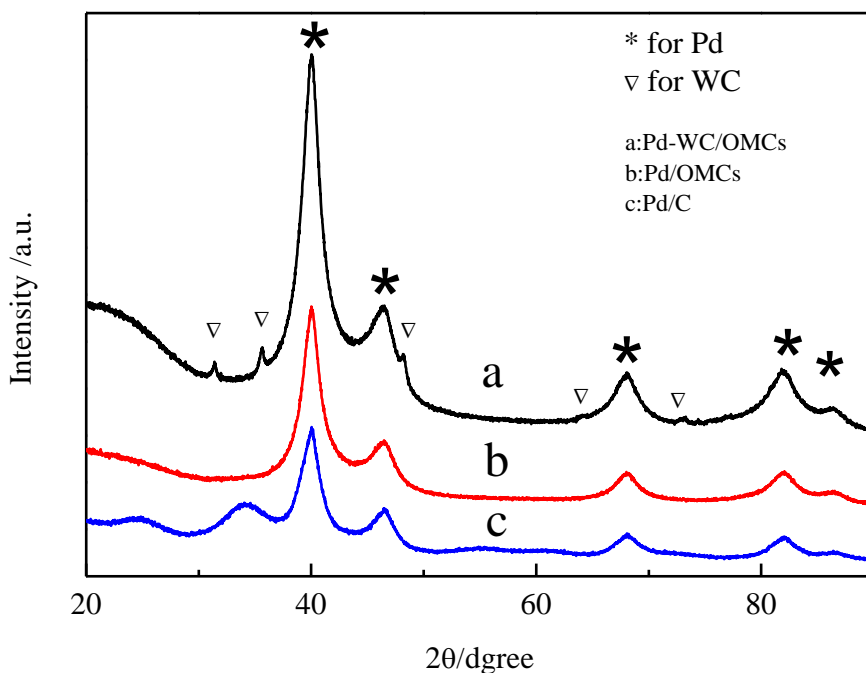


Figure 4. XRD patterns of Pd-WC/OMCs, Pd/OMCs and Pd/C.

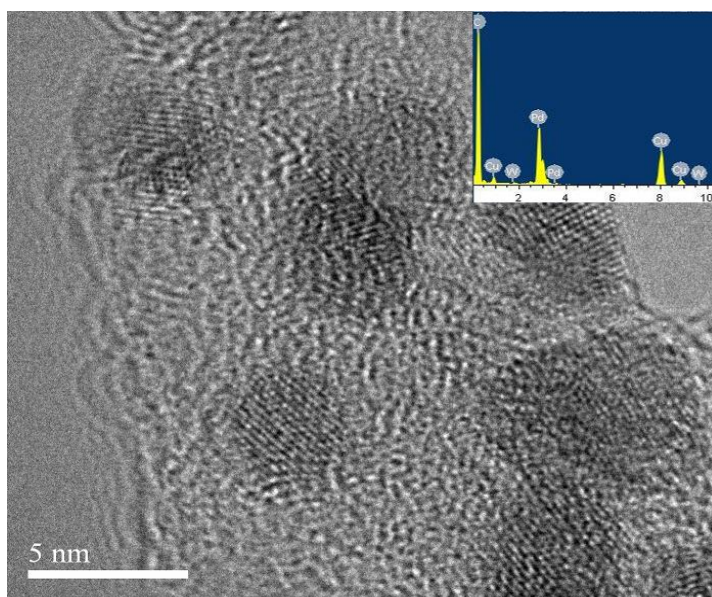


Figure 5. TEM image of Pd-WC/OMCs. The inset shows the EDS pattern of the sample.

Fig. 4 shows XRD patterns of as-prepared Pd-WC/OMCs, Pd/OMCs and commercial Pd/C (from BASF). Except for the characteristic peaks of WC in the case of Pd-WC/OMCs, all the XRD patterns clearly show the five main characteristic peaks of face-centred cubic (fcc) crystalline Pd, with lattice planes aligned at (1 1 1), (2 0 0), (2 2 0), (3 1 1) and (2 2 2). According to Scherrer's equation,

the estimated average Pd particle sizes using the fitted (2 2 0) plane are 5.3 nm for Pd/OMCs, 5.1 nm for Pd-WC/OMCs, and 5.5 nm for Pd/C. Figure 5 is a typical TEM image of the Pd-WC/OMCs; one finds that the Pd nanoparticles are uniformly dispersed on the pore surface of WC/OMCs with an mean particle diameters of ca. 5 nm, which is in fairly good agreement with the XRD results. Moreover, the EDS analysis (see the inset in Fig. 5) of the sample demonstrates the existence of Pd, W and C species.

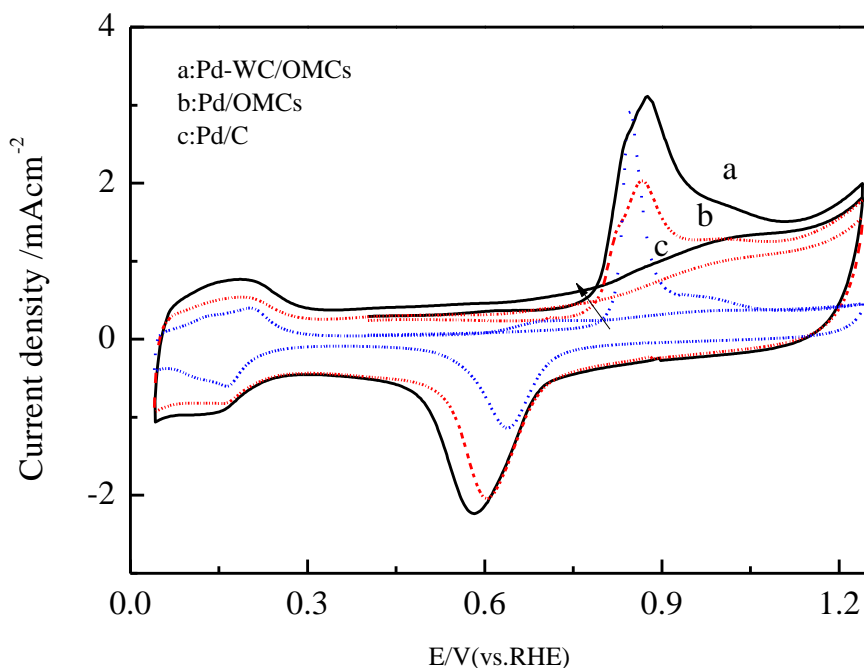


Figure 6. CO-stripping voltammograms for Pd-WC/OMCs, Pd/OMCs and Pd/C catalysts in 0.1M HClO₄ at scan rate of 20 mVs⁻¹.

Figure 6 shows CO-stripping voltammograms of Pd-WC/OMCs, Pd/OMCs and commercial Pd/C catalysts in 0.1M HClO₄ at scan rate of 20 mVs⁻¹. ECSA calculated from CO desorption area (ECSA-CO) are 24.13, 15.88 and 11.44 m²g⁻¹ for the Pd-WC/OMCs, Pd/OMCs and Pd/C catalysts, respectively. The onset potential for CO oxidation varies in the order Pd-WC/OMCs < Pd/OMCs < Pd/C, suggesting that adsorbed CO is prone to be oxidized on the Pd-WC/OMCs at lower potential, which may be ascribed to the WC resistance to CO poisoning and its Pt-like behavior in catalytic reactions [12,14].

A comparison of electrocatalytic activity of HCOOH oxidation on the WC/OMCs, Pd/OMCs, and commercial Pd/C catalysts is provided in Fig.7. No current peaks of HCOOH oxidation can be observed on the WC/OMCs, indicating that the WC/OMCs is inactive for HCOOH oxidation. For a typical curve of Pd-WC/OMCs catalysts, upon scanning from 0 V to positive potentials, the main oxidation peak potential occurs at 0.566 V and the corresponding peak current density occurs at 32.82 mAcm⁻², which is more than twice that of the Pd/C catalysts (14.01 mAcm⁻²) and higher than that on the Pd/OMCs (22.74mAcm⁻²). Moreover, the onset potentials on Pd-WC/OMCs and Pd/OMCs are slightly shifted toward the negative direction. These comparisons suggest that the decoration of Pd by WC, as well as the application of OMCs as a support material can improve the catalytic activity of Pd

significantly. In addition, it should be mentioned that the curve at Pd-WC/OMCs and Pd/OMCs catalyst electrode in Fig. 7 is not smooth because a large amount of CO_2 , the product of formic acid oxidation, escapes from the electrode surface. To further evaluate the activity and stability of the catalysts, the catalytic electrodes were polarized at 0.3 V/RHE in the solution of 0.1 M HCOOH + 0.1 M HClO_4 .

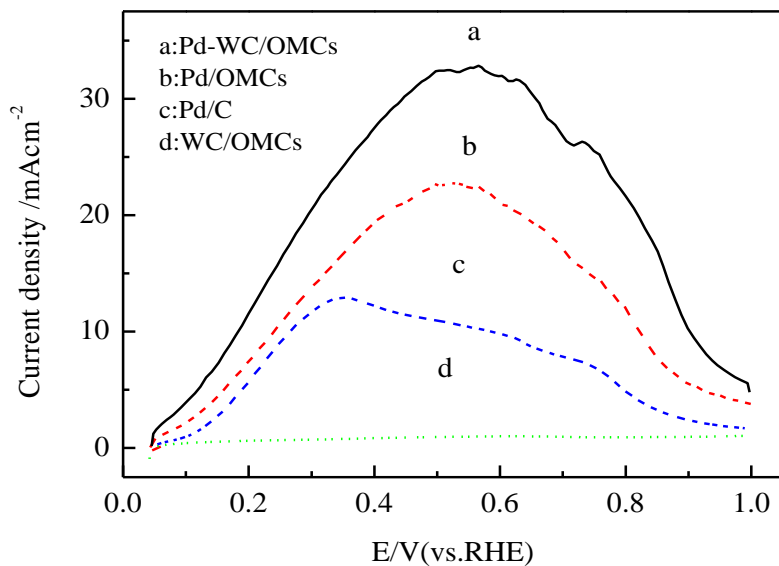


Figure 7. Cyclic voltammograms of the four catalysts in 0.1M HCOOH +0.1M HClO_4 solution at scan rate of 50 mVs^{-1} .

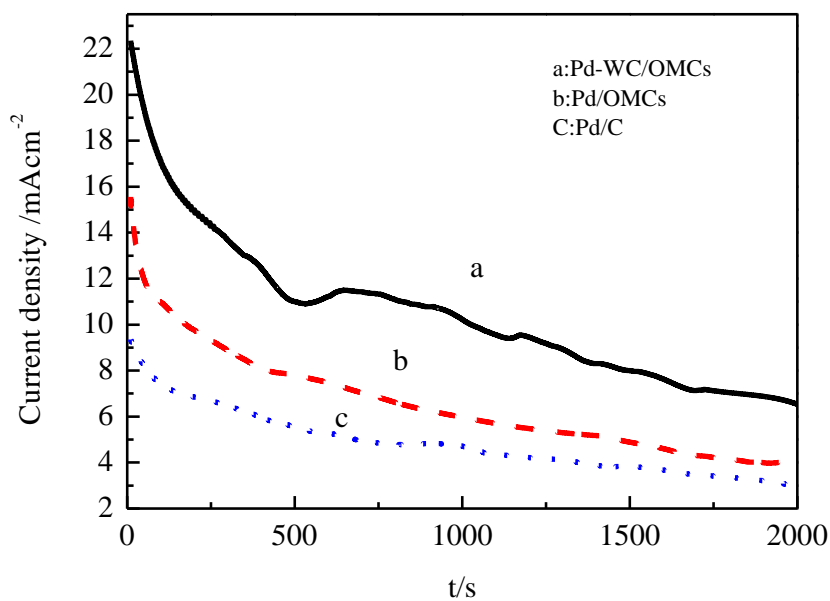


Figure 8. Chronamperometric curves of the catalysts (see Fig. in 0.1M HCOOH +0.1M HClO_4 solution at 0.3V/RHE).

Figure 8 shows the chronoamperometric curves of formic acid oxidation on Pd-WC/OMCs, Pd/OMCs and Pd/C catalysts. For all the catalysts, the current density decreases with time, which is a typical behavior pattern for Pd-based catalysts toward formic acid oxidation. Nonetheless, the Pd-WC/OMCs catalyst presents a higher current density than the Pd/OMCs and Pd/C catalysts over the whole process, indicating that Pd-WC/OMCs catalysts possess better activity as well as good stability during the formic acid oxidation process.

4. CONCLUSIONS

Pd nanoparticles supported on tungsten carbides embedded onto OMCs (Pd-WC/OMCs) were prepared by a hard template method. Activity comparisons of HCOOH oxidation on different catalysts with a similar Pd particle size indicate that the catalytic activity changes in the order of Pd-WC/OMCs > Pd/OMCs > Pd/C. Moreover, the catalytic activity on the Pd-WC/OMCs have current densities that are more than twice that of the commercial Pd/C. The significant increase in the catalytic activity of the Pd-WC/OMCs can be attributed to a synergistic effect between Pd nanoparticles, the WC support, as well as structural effects due to the OMCs.

ACKNOWLEDGEMENTS

This work was supported by the National Basic Research Program of China (973 Program, 2012CB932800), the Natural Science Foundation of China (21073219), Shanghai Science and Technology Committee (12ZR1431200 and 11DZ1200400) and the Knowledge Innovation Engineering of the CAS (12406, 124091231).

References

1. C. Rice, S. Ha, R. I. Masel, P. Waszczuk, A. Wieckowski and T. Barnard, *J Power Sources*, 111 (2002) 83.
2. C. Rice, S. Ha, R. I. Masel and A. Wieckowski, *J Power Sources*, 115 (2003) 229.
3. P. Waszczuk, T. M. Barnard, C. Rice, R. I. Masel and A. Wieckowski, *Electrochem Commun*, 4 (2002) 599.
4. C. T. Liu, M. Chen, C. Y. Du, J. Zhang, G. P. Yin, P. F. Shi and Y. R. Sun, *Int J Electrochem Sc*, 7 (2012) 10592.
5. W. P. Zhou, A. Lewera, R. Larsen, R. I. Masel, P. S. Bagus and A. Wieckowski, *J Phys Chem B*, 110 (2006) 13393.
6. J. Ge, W. Xing, X. Xue, C. Liu, T. Lu and J. Liao, *J Phys Chem C*, 111 (2007) 17305.
7. J. T. Zhang, C. C. Qiu, H. Y. Ma and X. Y. Liu, *J Phys Chem C*, 112 (2008) 13970.
8. X. M. Wang and Y. Y. Xia, *Electrochem Commun*, 10 (2008) 1644.
9. X. Wang, Y. Tang, Y. Gao and T. H. Lu, *J Power Sources*, 175 (2008) 784.
10. X. W. Yu and P. G. Pickup, *J Power Sources*, 192 (2009) 279.
11. L. L. Zhang, Y. W. Tang, J. C. Bao, T. H. Lu and C. Li, *J Power Sources*, 162 (2006) 177.
12. J.-Y. Wang, Y.-Y. Kang, H. Yang and W.-B. Cai, *J Phys Chem C*, 113 (2009) 8366.
13. R. B. Levy and M. Boudart, *Science*, 181 (1973) 547.
14. R. Ganesan and J. S. Lee, *Angewandte Chemie International Edition*, 44 (2005) 6557.

15. M. K. Jeon, H. Daimon, K. R. Lee, A. Nakahara and S. I. Woo, *Electrochem Commun*, 9 (2007) 2692.
16. M. D. Obradovic, B. M. Babic, V. R. Radmilovic, N. V. Krstajic and S. L. Gojkovic, *Int J Hydrogen Energ*, 37 (2012) 10671.
17. M. Nie, H. Tang, Z. Wei, S. P. Jiang and P. K. Shen, *Electrochem Commun*, 9 (2007) 2375.
18. F. Hu, G. Cui, Z. Wei and P. K. Shen, *Electrochem Commun*, 10 (2008) 1303.
19. M. D. Obradovic, S. L. Gojkovic, N. R. Elezovic, P. Ercius, V. R. Radmilovic, L. D. Vracar and N. V. Krstajic, *J Electroanal Chem*, 671 (2012) 24.
20. M. Nie, P. K. Shen, M. Wu, Z. Wei and H. Meng, *J Power Sources*, 162 (2006) 173.
21. H. Chhina, S. Campbell and O. Kesler, *J Power Sources*, 179 (2008) 50.
22. N. R. Elezovic, B. M. Babic, L. Gajic-Krstajic, P. Ercius, V. R. Radmilovic, N. V. Krstajic and L. M. Vracar, *Electrochim Acta*, 69 (2012) 239.
23. G. Li, C. a. Ma, J. Tang and Y. Zheng, *Mater Lett*, 61 (2007) 991.
24. S. Shanmugam, D. S. Jacob and A. Gedanken, *The Journal of Physical Chemistry B*, 109 (2005) 19056.
25. S. V. Pol, V. G. Pol and A. Gedanken, *Adv Mater*, 18 (2006) 2023.
26. Y. Wang, S. Song, V. Maragou, P. K. Shen and P. Tsiakaras, *Applied Catalysis B: Environmental*, 89 (2009) 223.
27. R. Ganesan, D. J. Ham and J. S. Lee, *Electrochem Commun*, 9 (2007) 2576.
28. Y. Wang, C. He, A. Brouzgou, Y. Liang, R. Fu, D. Wu, P. Tsiakaras and S. Song, *J Power Sources*, 200 (2012) 8.
29. D.-W. Wang, F. Li, H.-T. Fang, M. Liu, G.-Q. Lu and H.-M. Cheng, *The Journal of Physical Chemistry B*, 110 (2006) 8570.
30. Z. Lei, L. An, L. Dang, M. Zhao, J. Shi, S. Bai and Y. Cao, *Micropor Mesopor Mat*, 119 (2009) 30.
31. J. R. C. Salgado, F. Alcaide, G. Álvarez, L. Calvillo, M. J. Lázaro and E. Pastor, *J Power Sources*, 195 (2010) 4022.
32. S.H. Liu, F.S. Zheng and J.R. Wu, *Appl Catal B-Environ*, 108 (2011) 81.
33. Z. P. Sun, X. G. Zhang, H. Tong, Y. Y. Liang and H. L. Li, *J Colloid Interf Sci*, 337 (2009) 614.
34. S. H. Joo, S. J. Choi, I. Oh, J. Kwak, Z. Liu, O. Terasaki and R. Ryoo, *Nature*, 412 (2001) 169.
35. D. Zhao, J. Feng, Q. Huo, N. Melosh, G. H. Fredrickson, B. F. Chmelka and G. D. Stucky, *Science*, 279 (1998) 548.
36. S. Jun, S. H. Joo, R. Ryoo, M. Kruk, M. Jaroniec, Z. Liu, T. Ohsuna and O. Terasaki, *J Am Chem Soc*, 122 (2000) 10712.
37. W. He, J. Y. Liu, Y. J. Qiao, Z. Q. Zou, X. G. Zhang, D. L. Akins and H. Yang, *J Power Sources*, 195 (2010) 1046.